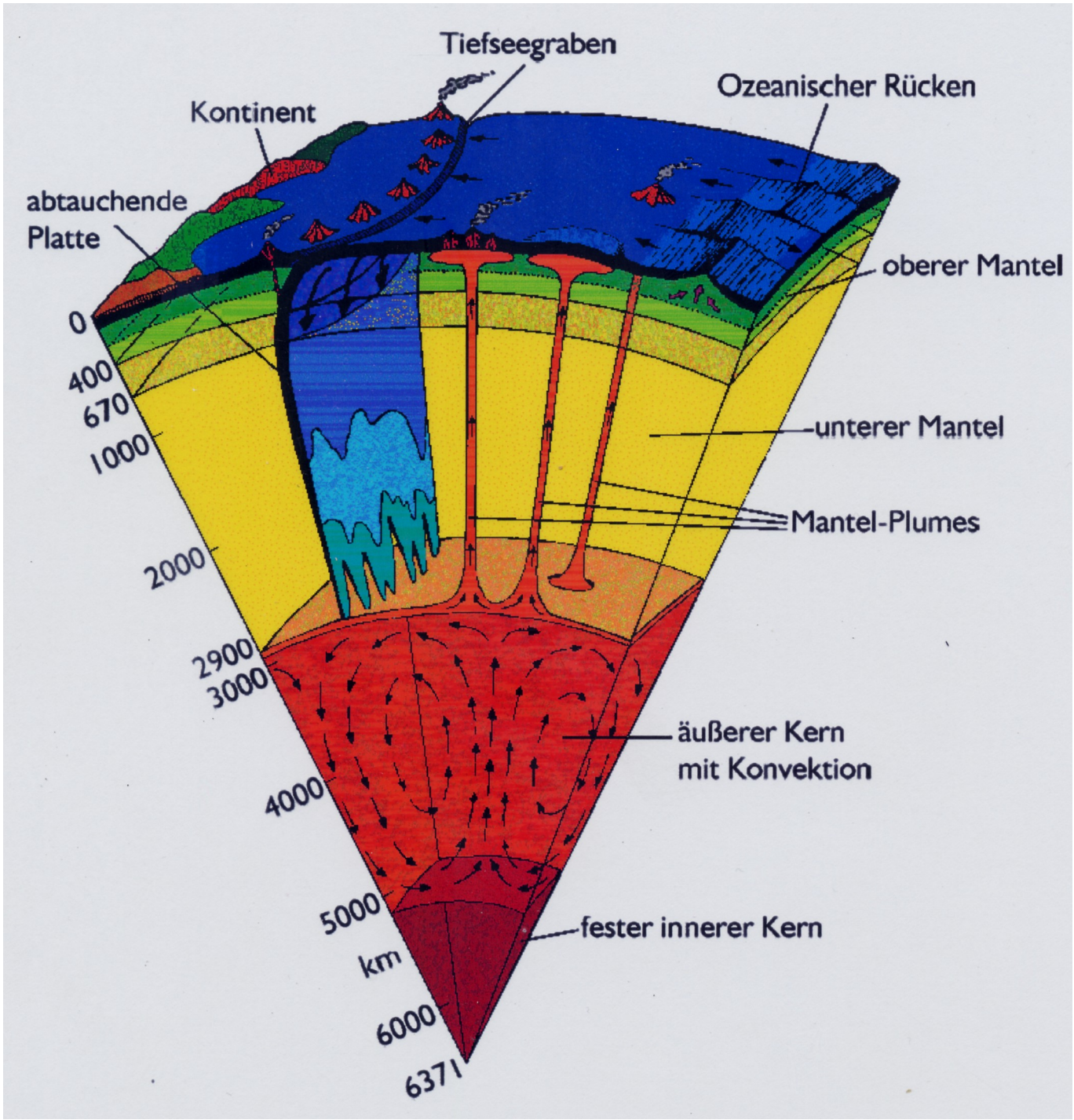
Tiefseegraben
Ozeanischer Rücken
Kontinent
abtauchende Platte
oberer Mantel
0
400
670
1000
2000
2900
3000
4000
5000
km
6000
6371
unterer Mantel
Mantel-Plumes
äußerer Kern mit Konvektion
fester innerer Kern

Earth is a terrestrial planet,

but not a typical one.

[Anonymous]

1. Seismology and internal structure

1.1 Fundamentals

Body waves
- P-waves: $v_P = \sqrt{\frac{k + \frac{4}{3}\mu}{\rho}}$
- S-waves: $v_S = \sqrt{\frac{\mu}{\rho}}$

k: incompressibility μ: shear modulus ρ: density

Surface waves
- Rayleigh waves
- Love waves

Dispersion $v(\lambda)$!

Free oscillations
- spheroidal
- toroidal

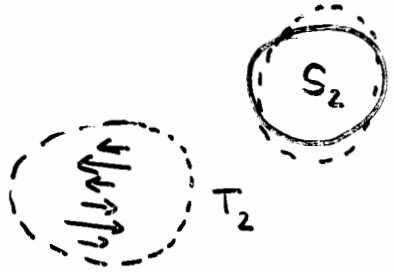

Earth: longest mode ${}_0S_2$: 54 min

Period depends on $v_P(r)$, $v_S(r)$, $\rho(r)$!

1.2 Body wave propagation in a spherically symmetric Earth

Continuous variation $v_P(r)$, $v_S(r)$
→ curved ray paths

At discontinuities: Refraction, Reflexion,
Conversion (P→S, S→P)

Seismic phases P, S, K: P-phase in core
PcP: reflected from core
PPP: twice reflected at surface

- For radial symmetry, the travel time for a phase is only a function of epicentral distance!

- Evidence for core with reduced v_p: „Shadow zone" between $\Delta = 103°$ and $\Delta = 142°$
- Now S-waves in (outer) core → liquid.
- Weak PKIKP-arrivals in shadow zone → inner core (solid)
- Knowledge of $T(\Delta)$ allow determination of epicenter when 3 observations for an earthquake
- inversion of $T(\Delta)$ → $v_p(r)$, $v_s(r)$

1.3 Earth structure

Crust	Oceanic	7 km	Basalt	Ca, Al-rich
	Continental	~35 km	(Granite)	SiO_2-rich
Mantle		– 2890 km	Olivine	$(Mg_{0.9}Fe_{0.1})_2SiO_4$
Outer core		r = 3480 km	Fe (+Ni + light element) Liquid	
Inner core		r = 1220 km	Fe (+...)	solid

Mantle: weak discontinuities at 410, 660 km
solid – solid phase transitions of olivine

Density: not constrained by body waves
→ free oscillations (+ gravity + rotation data)

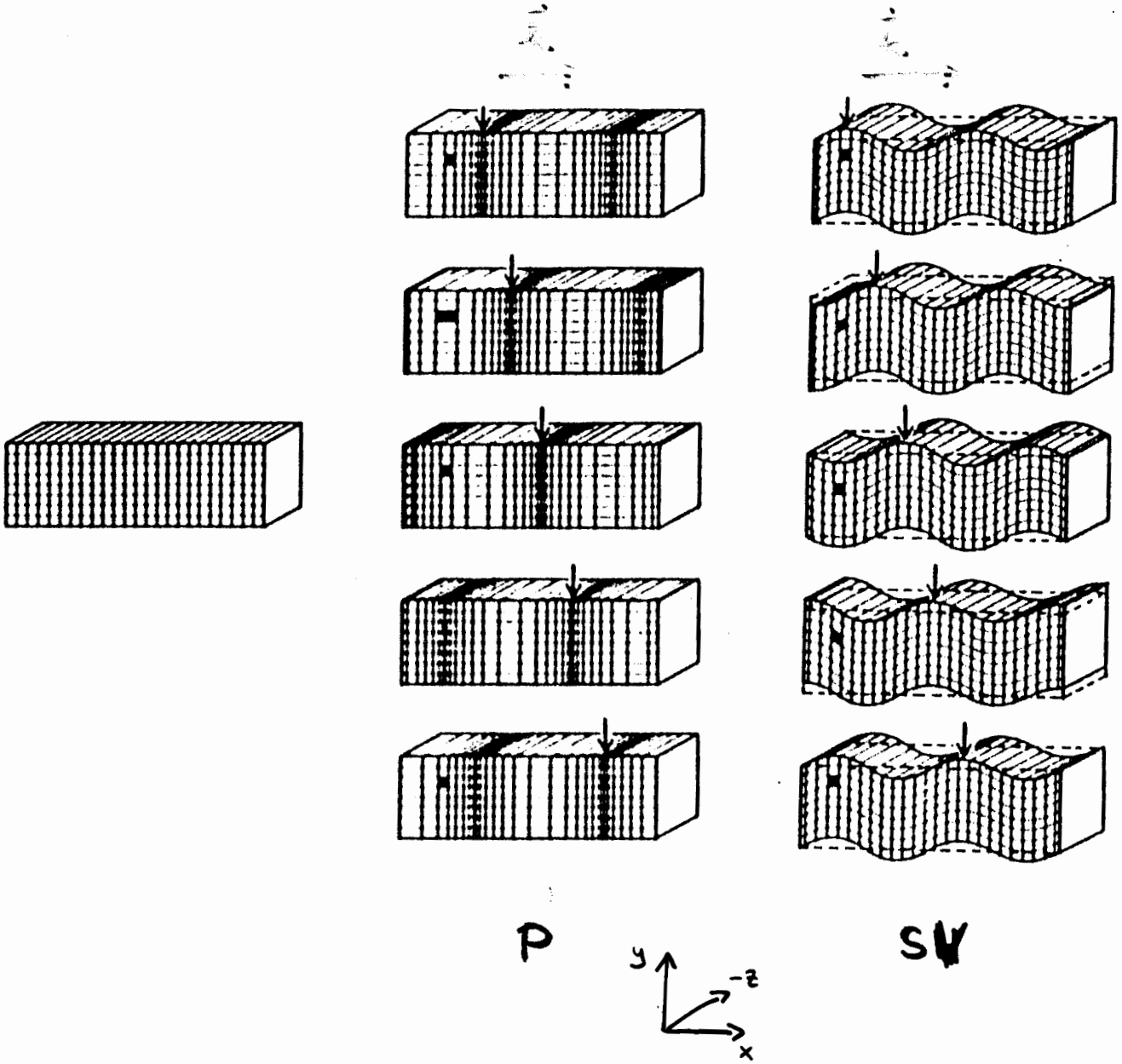
P
SV
y
-z
x

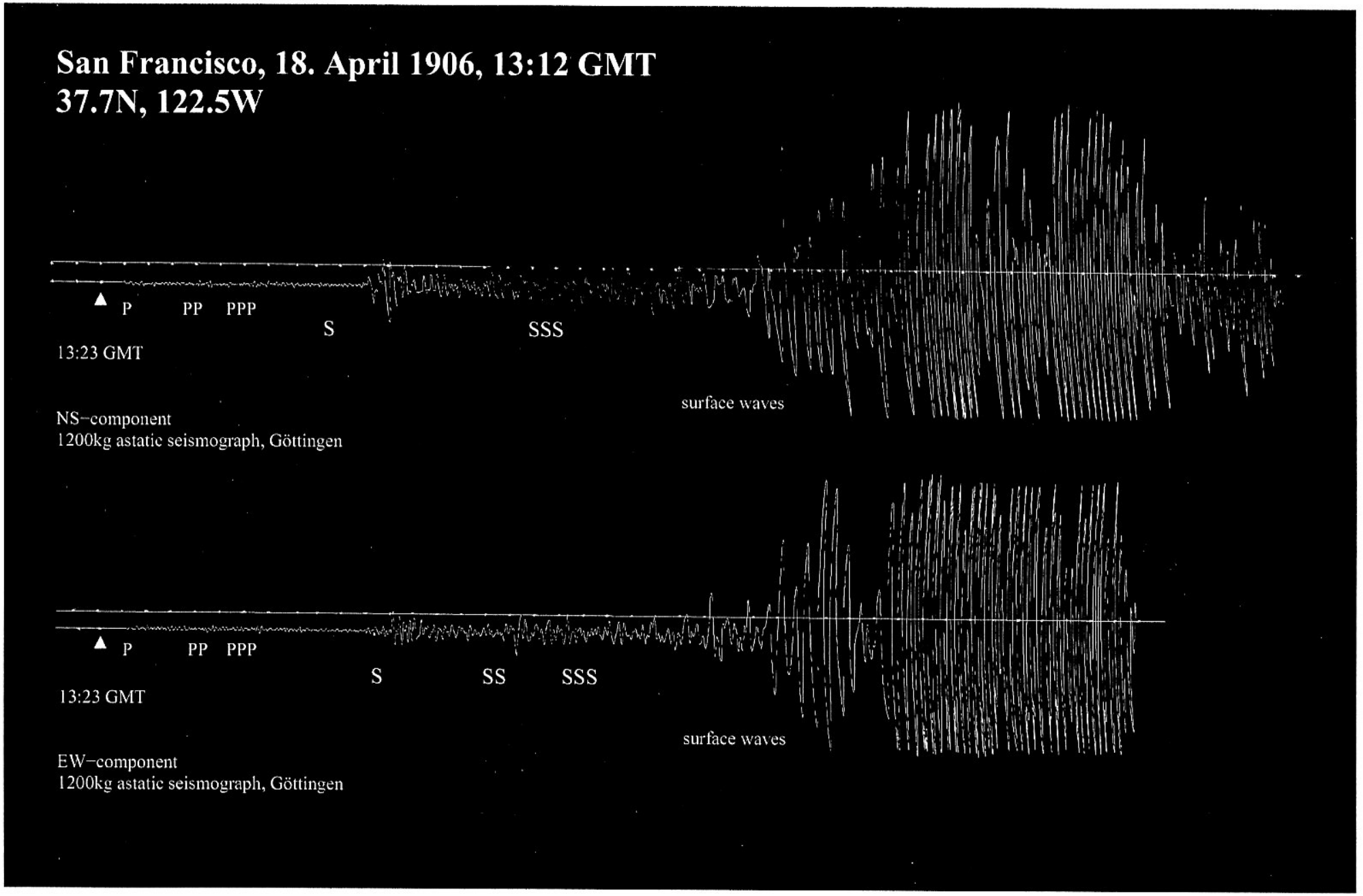
San Francisco, 18. April 1906, 13:12 GMT
37.7N, 122.5W
P
PP
PPP
S
SSS
13:23 GMT
surface waves
NS−component
1200kg astatic seismograph, Göttingen
P
PP
PPP
S
SS
SSS
13:23 GMT
surface waves
EW−component
1200kg astatic seismograph, Göttingen

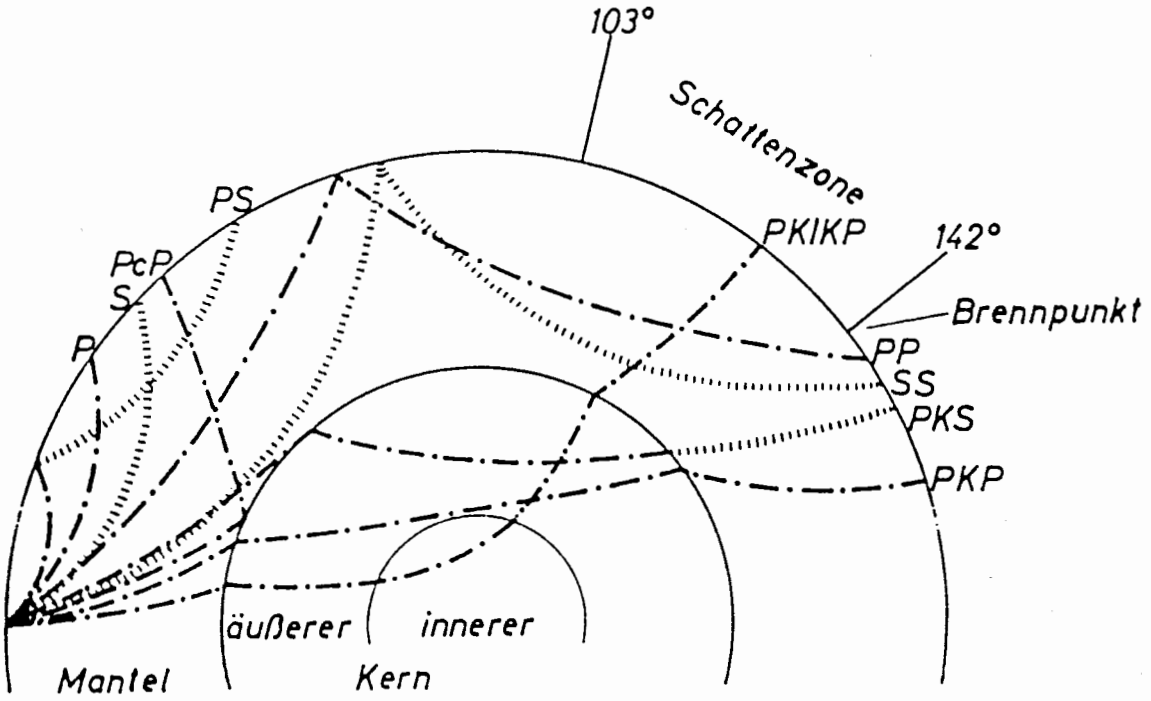
103°
Schattenzone
PS
PcP
S
P
PKIKP
142°
Brennpunkt
PP
SS
PKS
PKP
äußerer
innerer
Mantel
Kern

Seismische Raumwellenphasen:

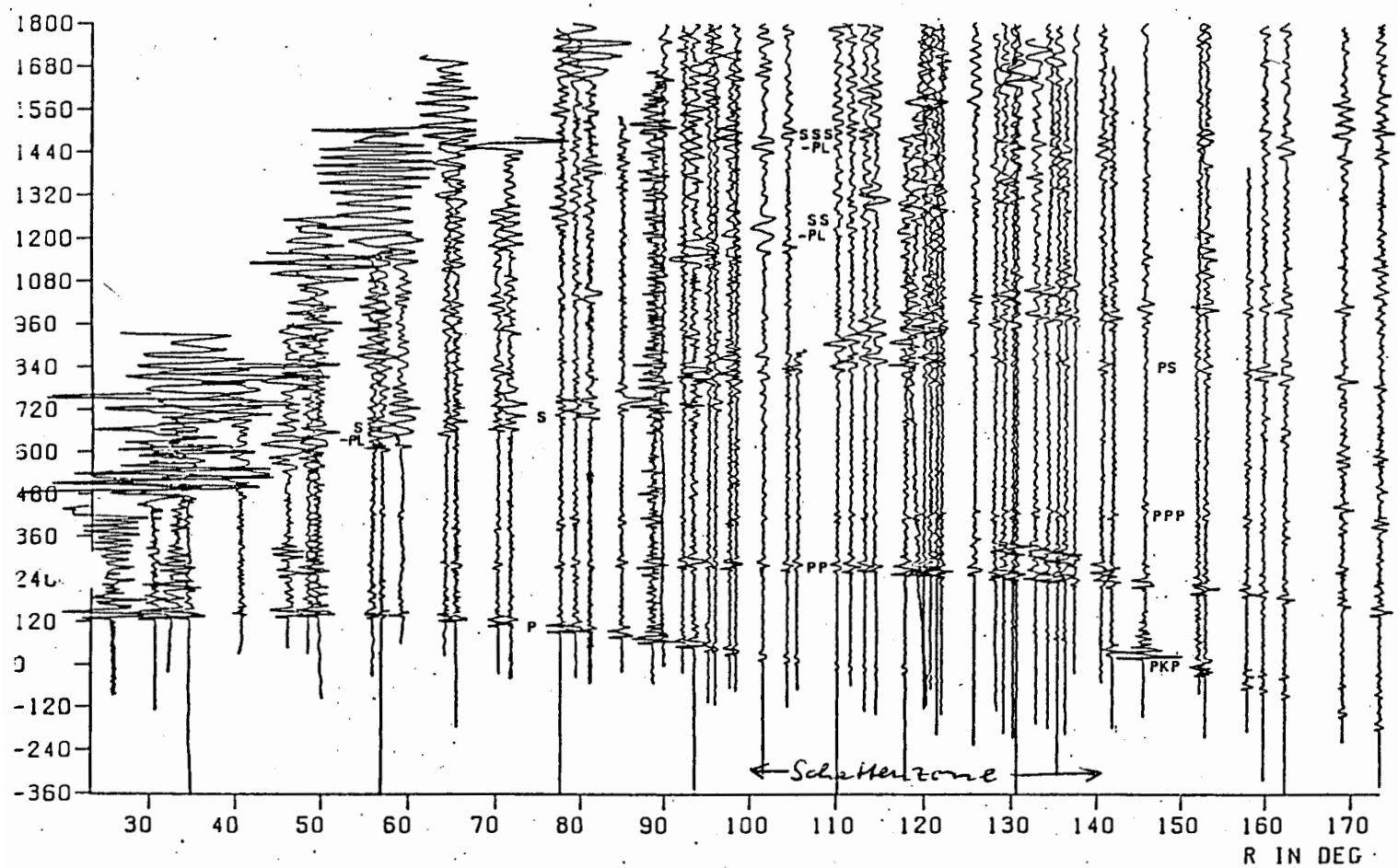

Vertical component seismogram section of an earthquake near Sumatra, recorded by WWNSS and CSN stations. Upward motion to the left. The amplitud scales of all traces are the same. See text for more details.

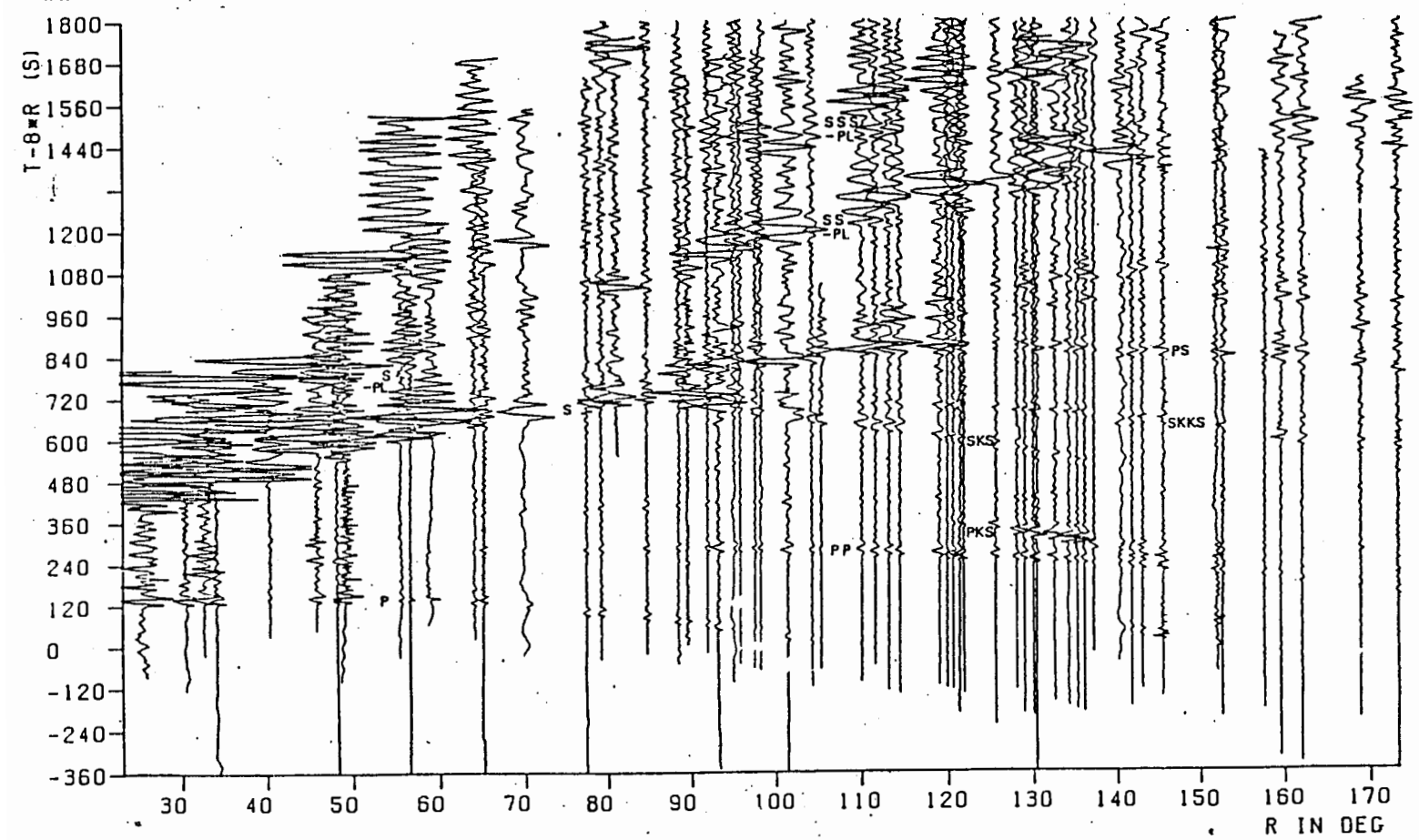

. 2. Radial component seismogram section of the same earthquake. Motion towards the epicentre to the left. Amplitude scale is the same as in Fig. 1.

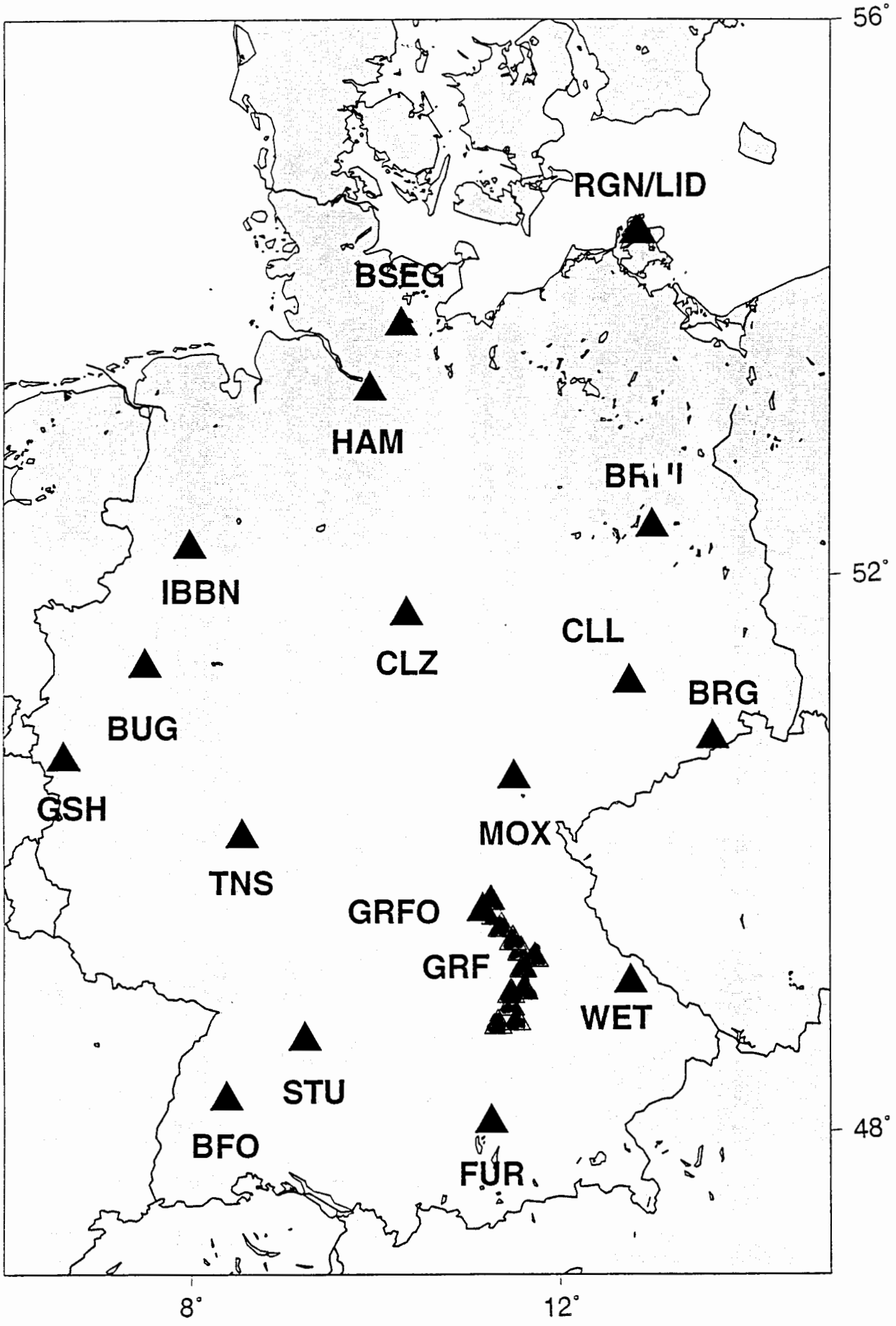
56°
52°
48°
8°
12°
RGN/LID
BSEG
HAM
BRH
IBBN
CLZ
CLL
BRG
BUG
GSH
MOX
TNS
GRFO
GRF
WET
STU
BFO
FUR

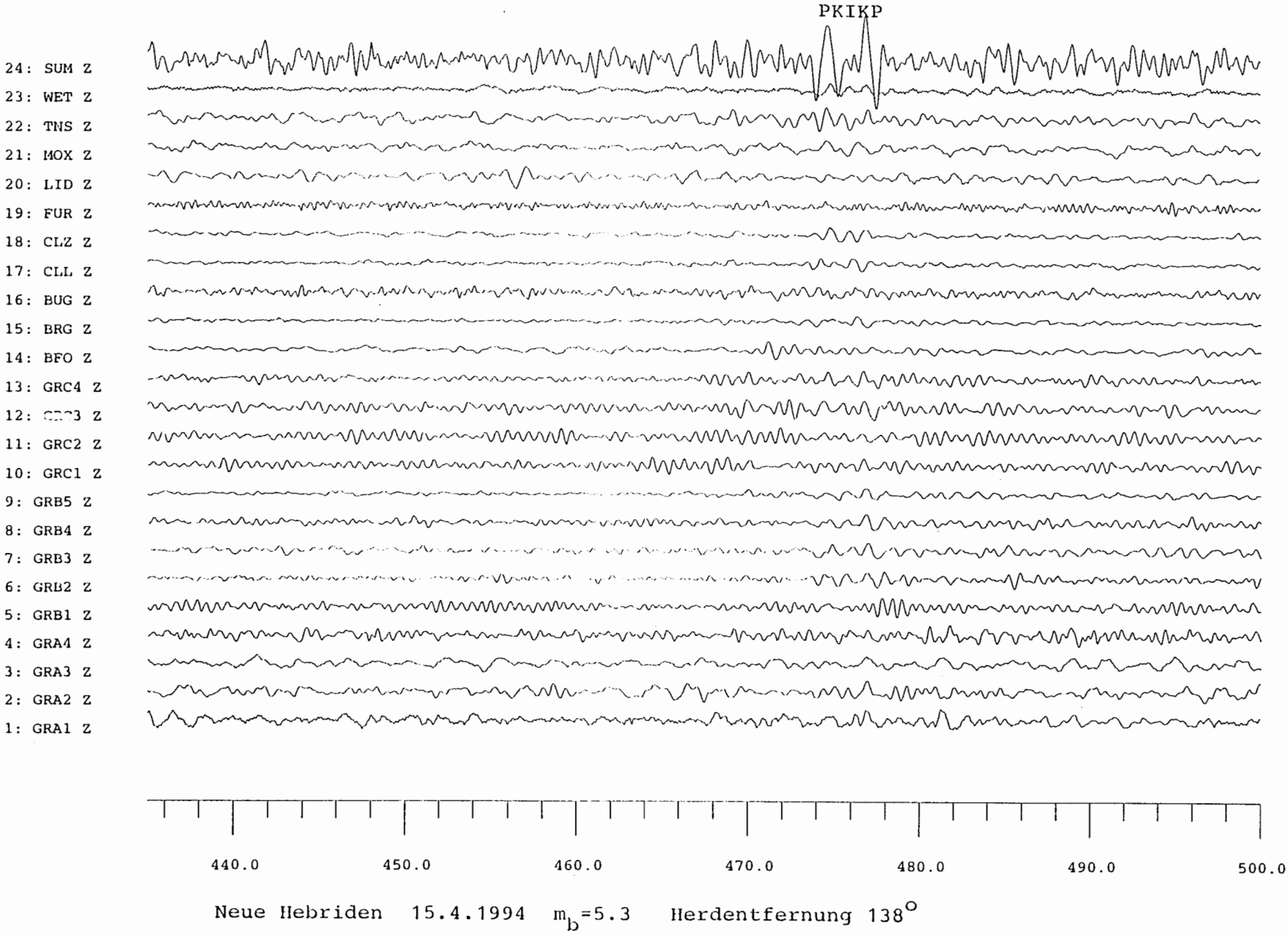

Neue Hebriden 15.4.1994 m_b=5.3 Herdentfernung 138°

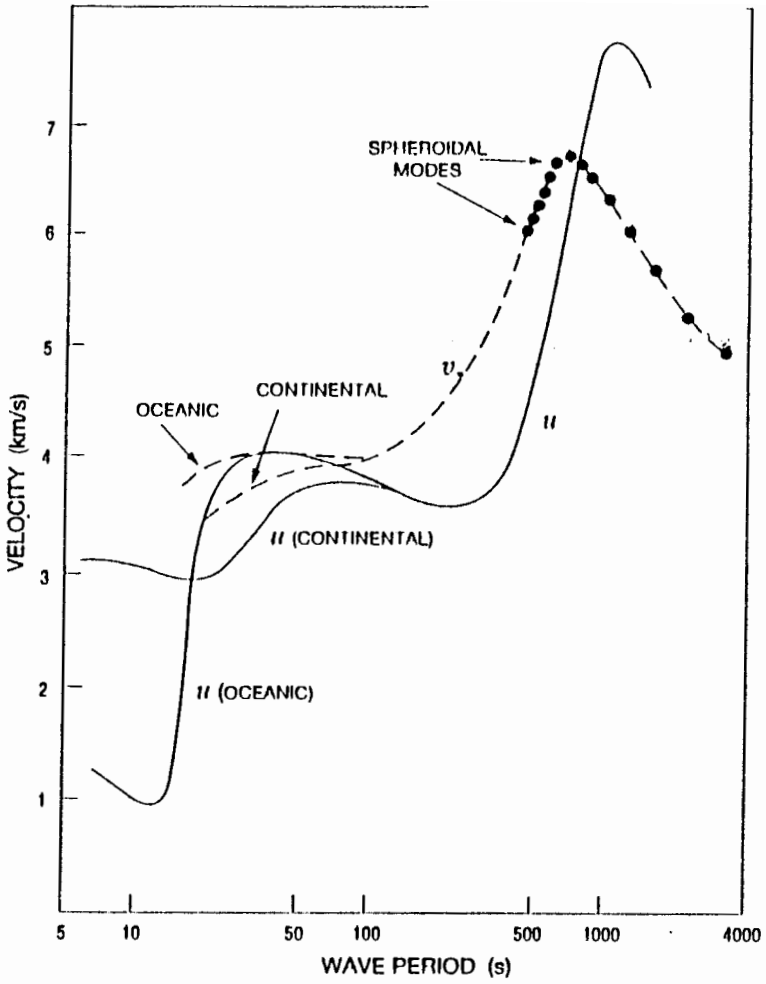

Figure 5.3(a). Fundamental mode Rayleigh wave dispersion. Group velocity, *u*, is shown by a solid line and inferred phase velocity, *v*, by a broken line, with the dispersion curve from free oscillation periods above 400s. Figure based on Oliver (1962).

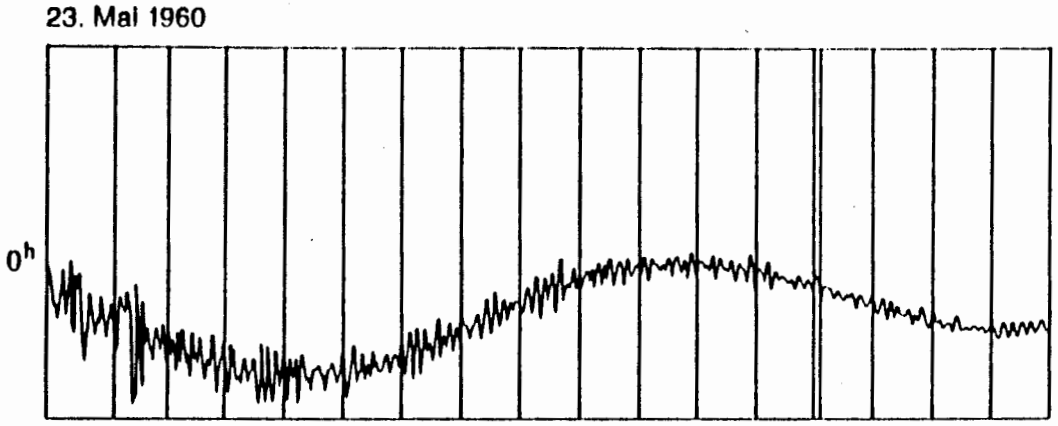

Abb. 5.45 Aufzeichnung des Ausschwingens der Erde nach dem großen Chile-Beben 1960. Die Schwingungen reiten auf der Gezeitenbewegung mit etwa halbtägiger Periodizität. Linienabstand 1 Stunde (nach Bolt 1982).

Blatt 8: Oben: Dispersionskurven für Rayleighwellen. u: Gruppengeschwindigkeit, v: Phasengeschwindigkeit (Stacey)
Unten: Registrierung von Eigenschwingungen der Erde (Berckhemer)

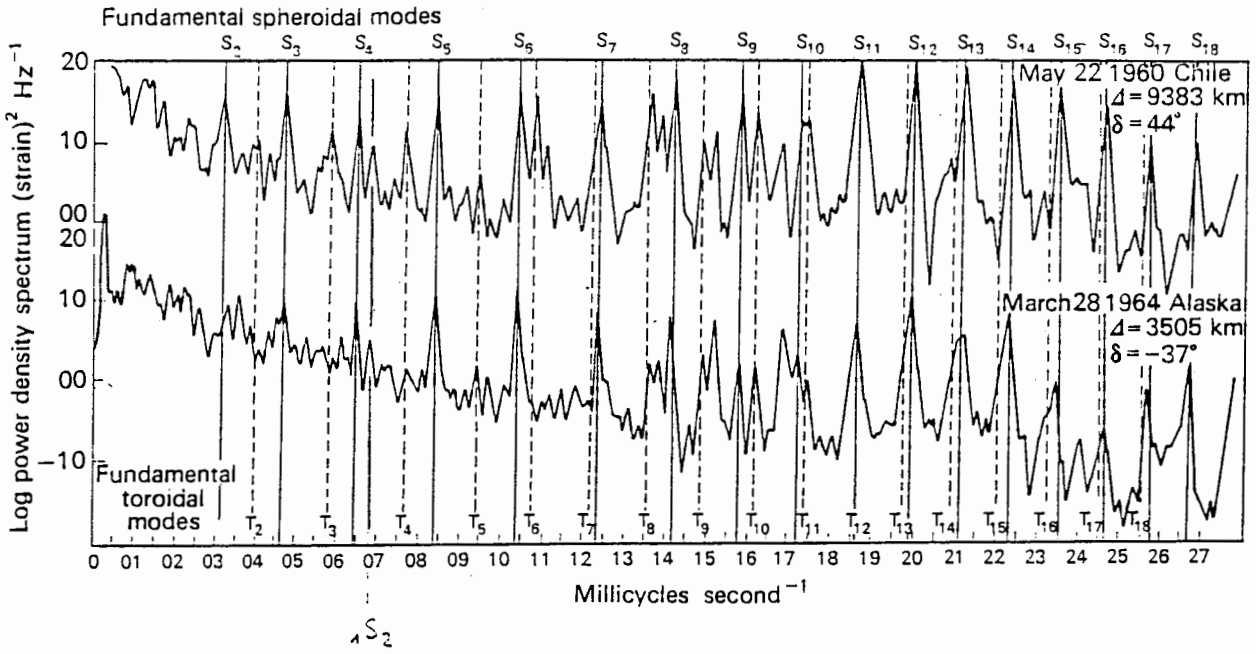

Fig. 4.9 Power spectral density of the Alaskan and Chilean earthquakes recorded on a strain seismometer at Isabella, California. The angle δ is the deviation of the great circle path from the axis of the strain seismometer. Redrawn from SMITH (1966), *J. geophys. Res.*, **71**, 1187.

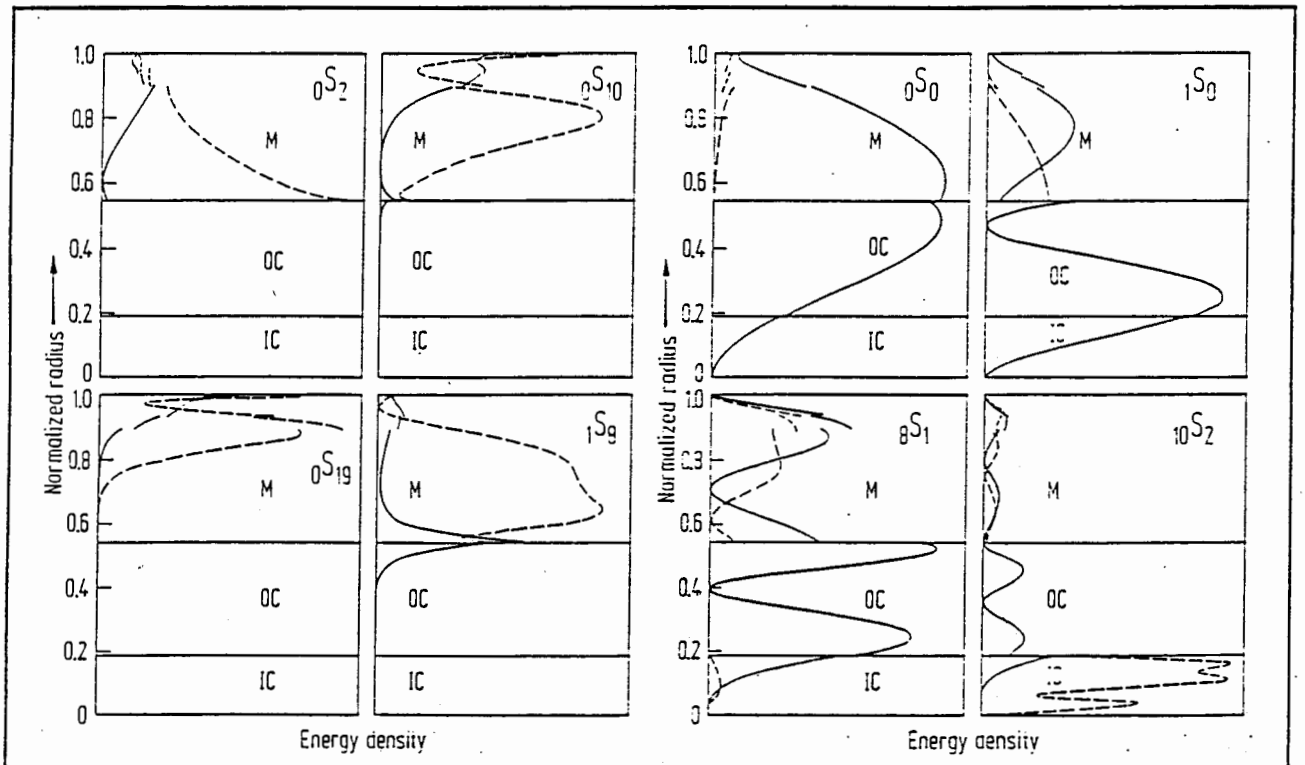

Fig. 15. Plots of compressional energy density (solid line) and shear energy density (broken line) as functions of normalized radius for modes ${}_0S_2$, ${}_0S_{10}$, ${}_0S_{19}$, ${}_1S_9$, ${}_0S_0$, ${}_1S_0$, ${}_8S_1$ and ${}_{10}S_2$ [80G]. The core-mantle boundary and the boundary between outer and inner core are indicated by solid horizontal lines. Energy densities are in relative units. (IC = inner core. OC = outer core. M = mantle.)

7 Earth models

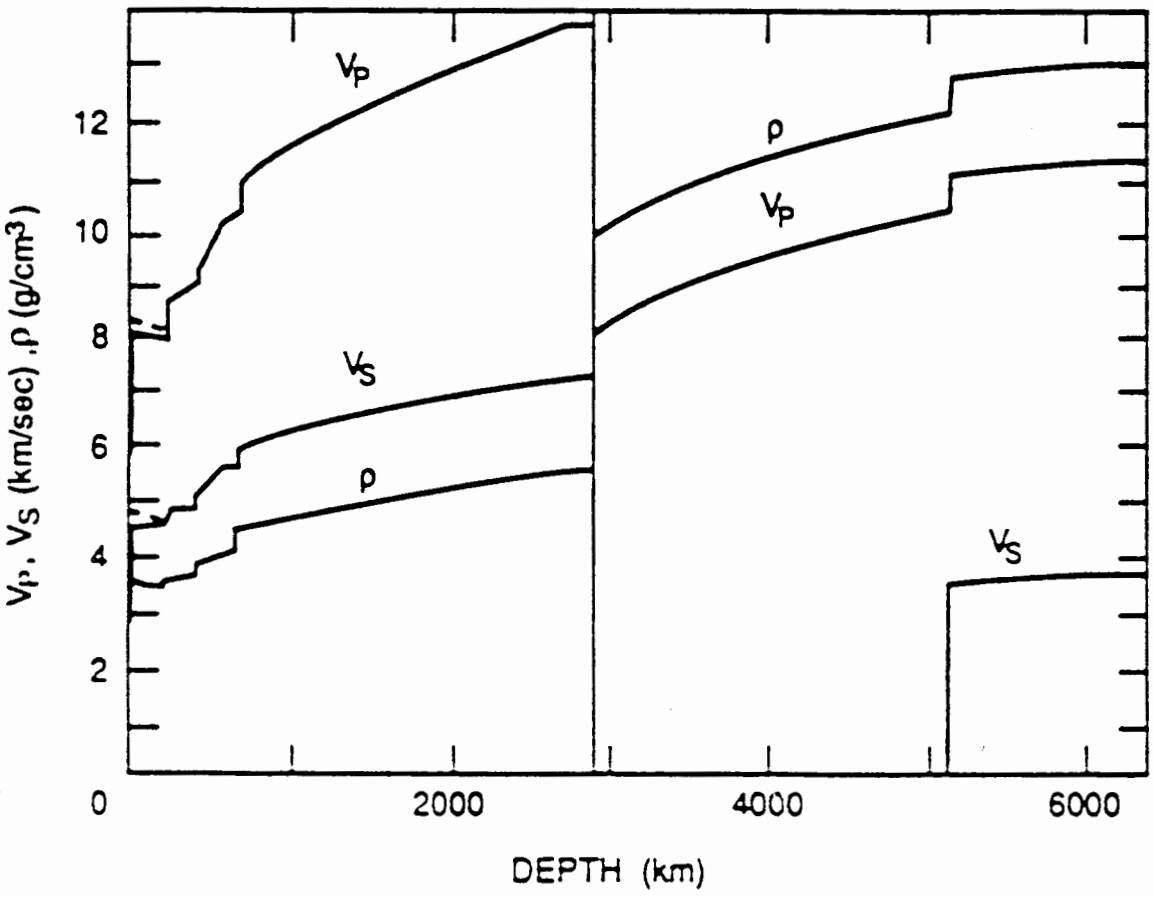

7.2. PREM model: Seismic velocities and density profile (after Dziewonski and Anderson 1981).

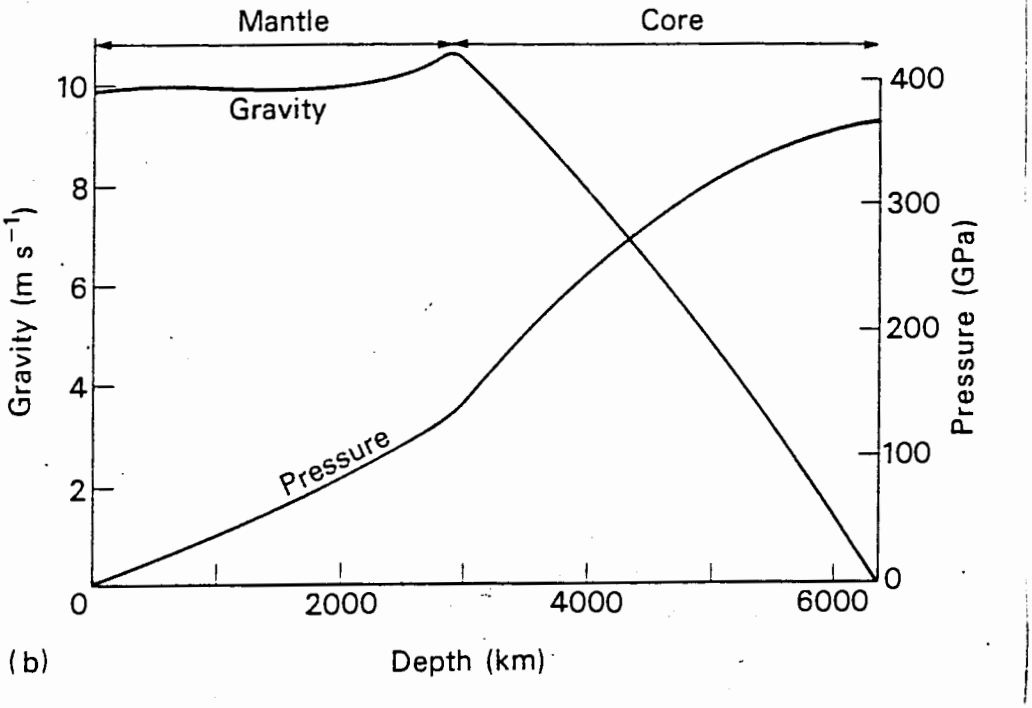

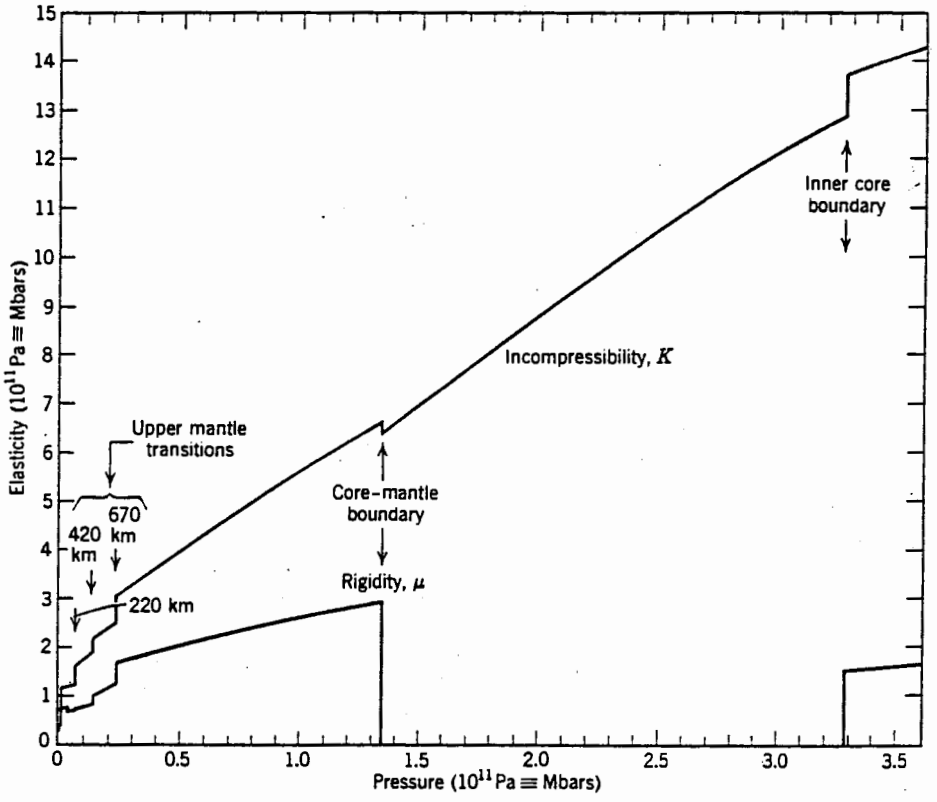

Figure 6.18. Variations of elastic constants with pressure in the interior of the Earth (model data by Dziewonski et al. 1975—Appendix G).

Chemical composition of Earth components

	Cont. Crust	Oceanic Crust	Mantle	Core
Thickness [km]	35 – 40	6 -7	2900	3500
Typical rock	Granit	Basalt	Peridotite	(Iron)
Density [kg/m^3]	2700	2900	3300	10,000
Composition [wt.-%]				
SiO_2	67	52	45	Fe: 85
MgO	2	10	39	Ni: 5-10
FeO	4	10	9	other
Al_2O_3	16	14	3	(O,S,Si,C,H…): 5-10
CaO	4	11	3	
other	7	3	1	
Main minerals				
	Quartz: SiO_2 Plagioclase: $CaAl_2Si_2O_8$ - $NaAlSi_3O_8$	Plagioclase Pyroxene: $CaMgSi_2O_6$ - $(Mg,Fe)SiO_3$	Olivine: $(Mg,Fe)_2SiO_4$ Pyroxene Garnet: $Mg_3Al_2Si_3O_{12}$	

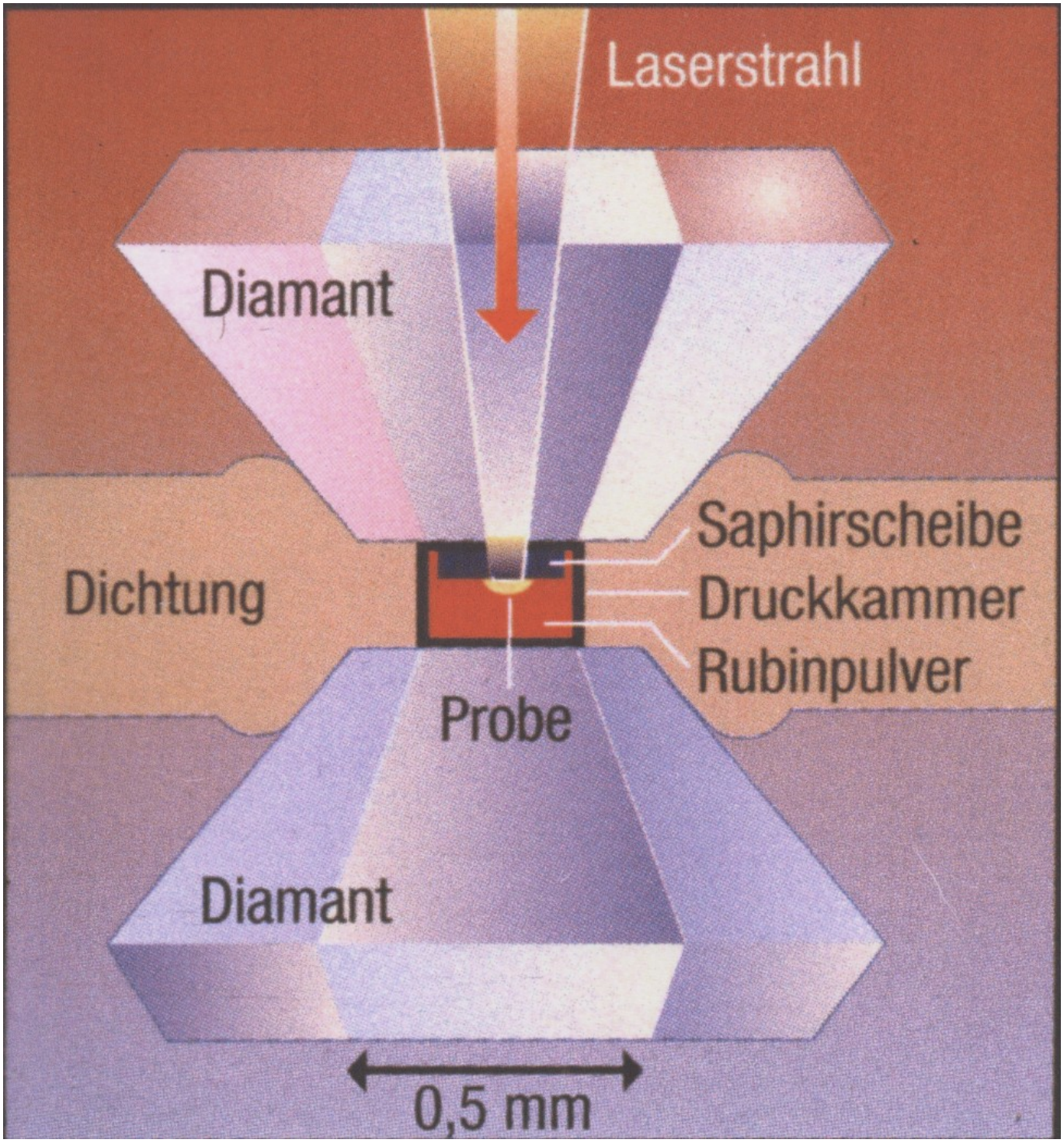
Laserstrahl
Diamant
Dichtung
Saphirscheibe
Druckkammer
Rubinpulver
Probe
Diamant
0,5 mm

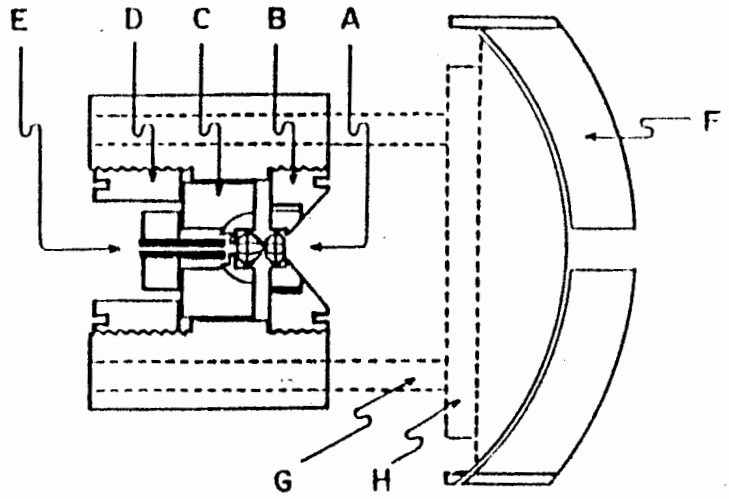

FIGURE 10-7
Cross section of diamond anvil press developed by Bassett et al., 1967. A—Diamond anvils; B—stationary piston; C—sliding piston; D—driver screw; E—collimator; F—film cassette; G—cassette mounting rods; H—cassette translating bars. (*From Bassett et al., 1967; with permission.*)

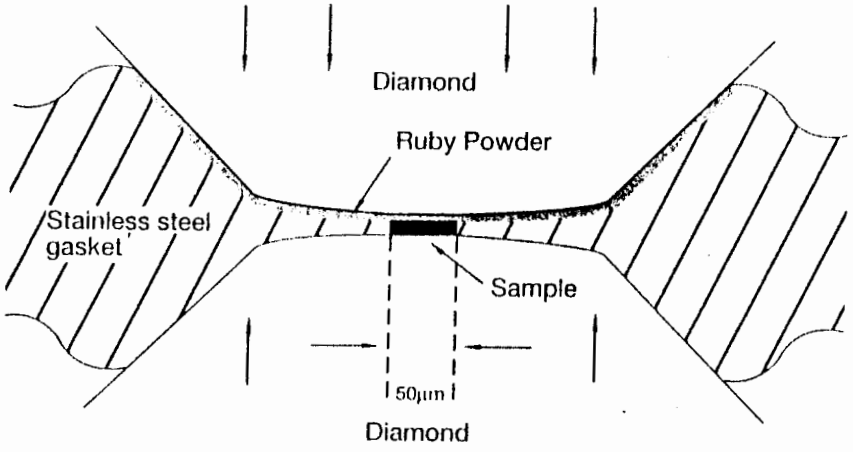

Figure 5.23. Configuration of the diamond anvil cell used by Goettel et al. (1985) to reach a static pressure of 280GPa at the centre of specimen in the form of a disc 50μm in diameter. The wavelength at which tiny fragments of ruby fluoresce is used as a measure of pressure.

Blatt 17 Diamant-Stempelpresse. Die Probe kann mittels eines fokussierten Lasers auf hohe Temperatur (mehrere tausend Kelvin) aufgeheizt werden. Die Frequenz der Fluoreszenzlinie von Rubinsplittern dient als Druckmaß, die Temperatur wird aus der emittierten Schwarzkörperstrahlung bestimmt. Kristallstruktur und Gitterkonstanten (-> Dichte) werden mittels Röntgenstrukturanalyse bestimmt. Neuere Entwicklungen schließen die Probe in "Druckkammer" in Argon ein, um angenähert hydrostatische Drucke zu erzeugen.

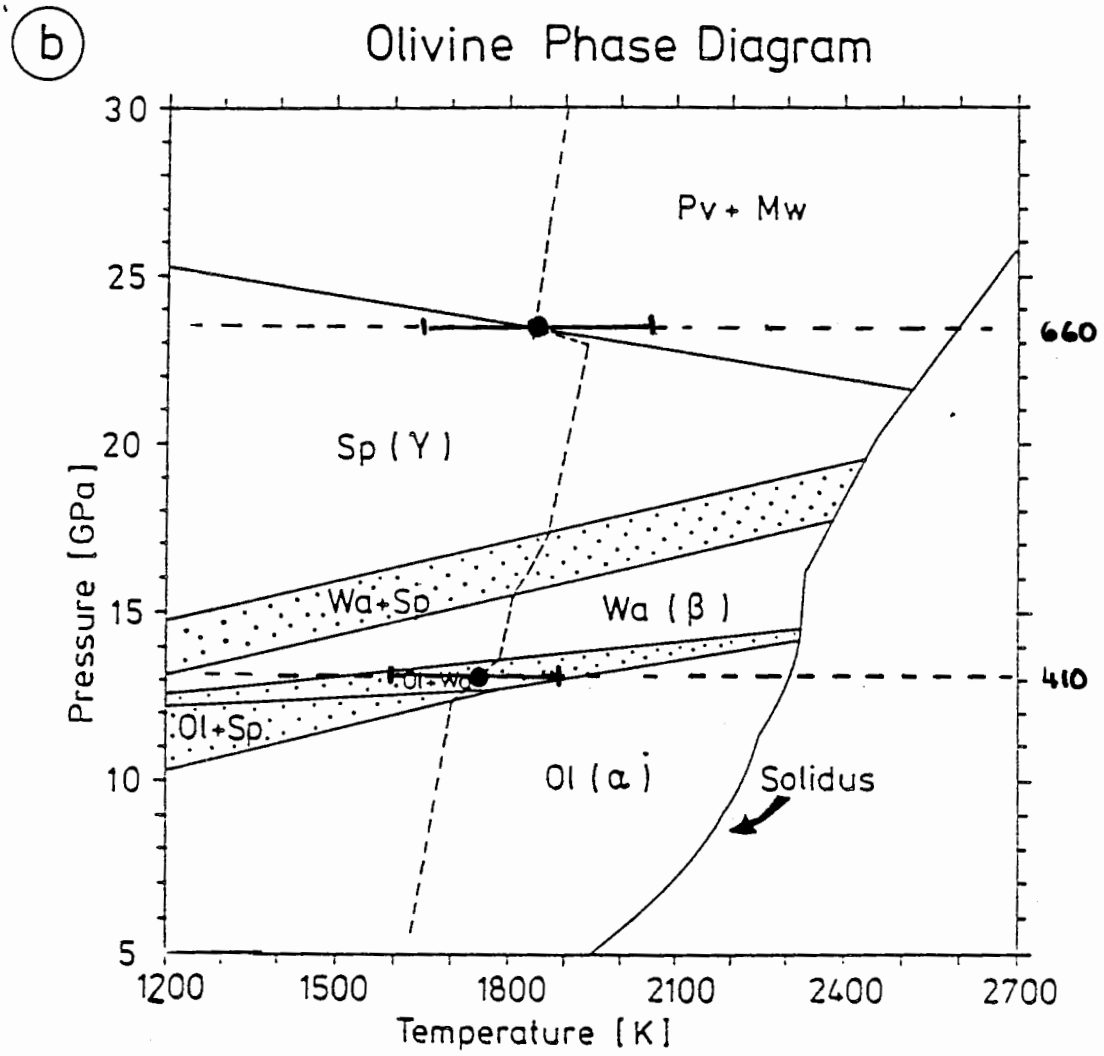
b
Olivine Phase Diagram
Pv + Mw
Sp (γ)
Wa+Sp
Wa (β)
Ol+Wa
Ol+Sp
Ol (α)
Solidus
660
410
Pressure [GPa]
Temperature [K]
30
25
20
15
10
5
1200
1500
1800
2100
2400
2700

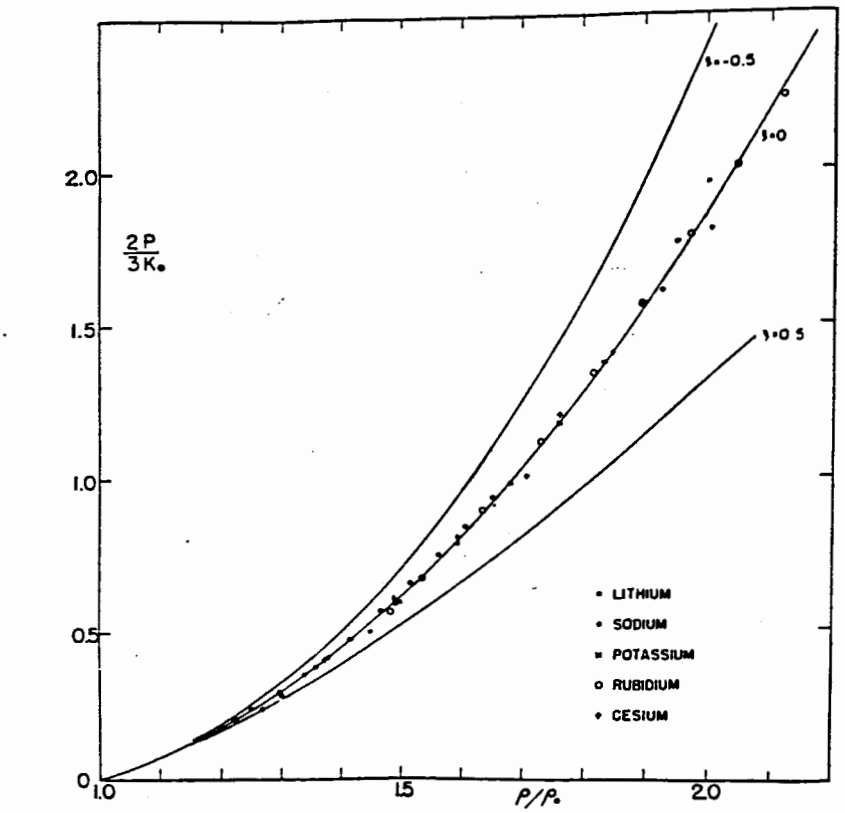

FIGURE 9-3
Experimental measurements of compressions of the alkali metals compared with compressions calculated from Birch-Murnaghan equation (13). (*From Birch, 1952, with permission.*)

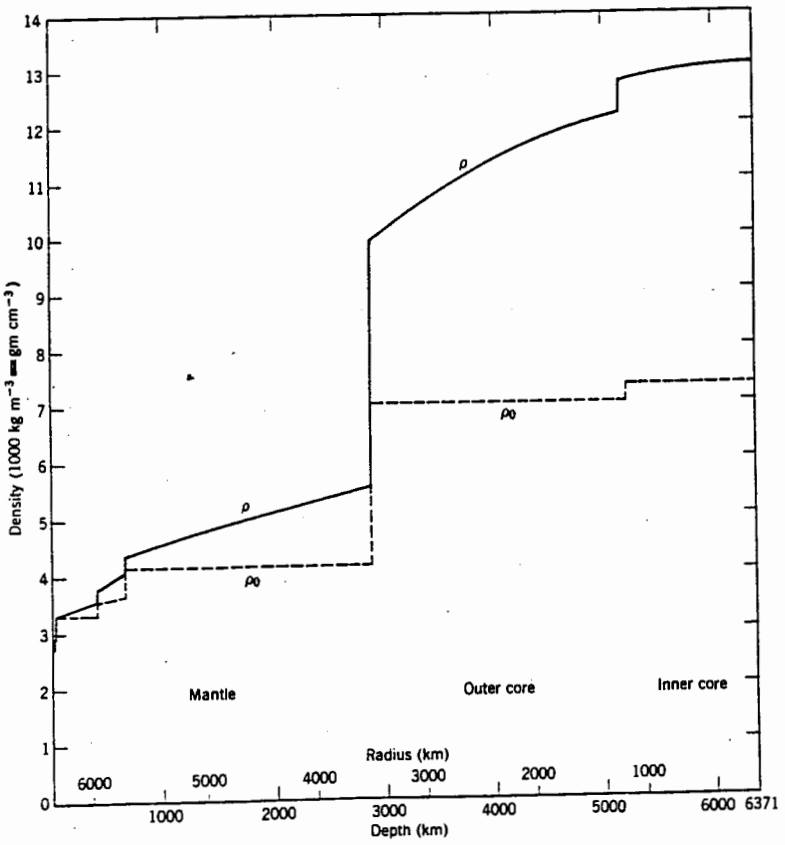

Figure 6.17. Density profile of Earth model by Dziewonski et al. (1975) (solid line) with corresponding extrapolated zero pressure (and room temperature) density (broken line).

a

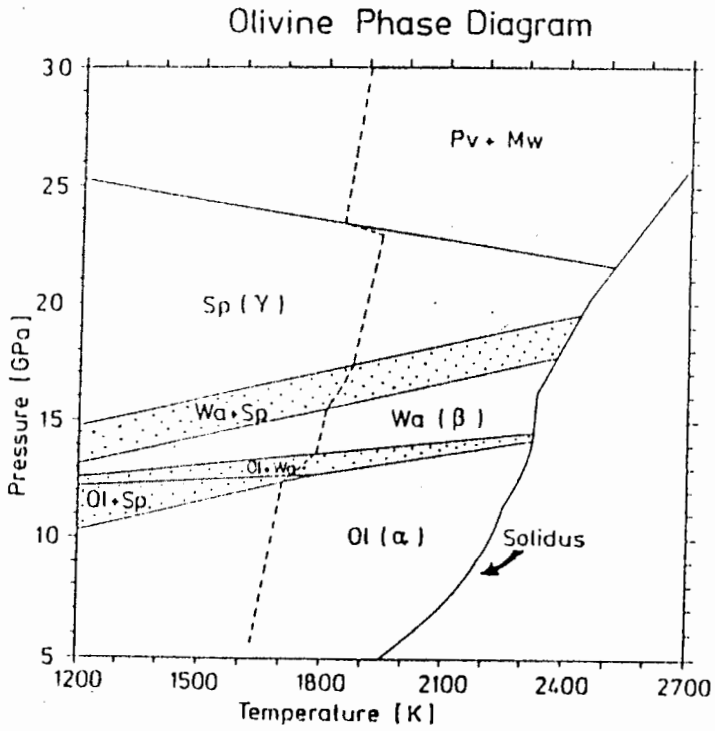

b

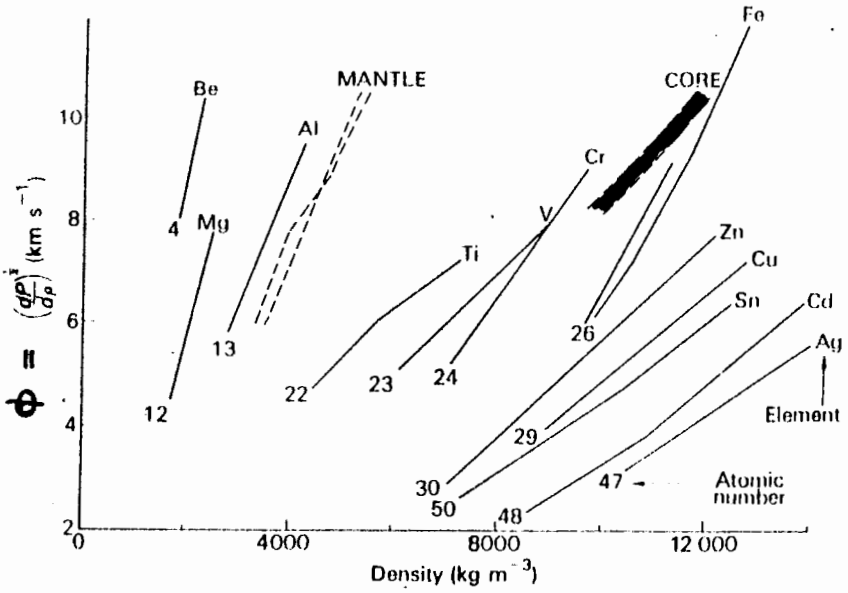

Fig. 6.6 Hydrodynamic sound velocity as a function of density shown for a selection of metals as obtained by shock wave experiments (solid lines) and for the mantle and core as obtained by seismic observations and density models (dashed lines). The numbers shown are atomic numbers. Redrawn from BIRCH (1961b), *Geophys. J. R. astr. Soc.*, **4**, 309.

Blatt 18

(a) Phasendiagramm von Olivin $(Mg_{0.9}Fe_{0.1})_2SiO_4$. Ol=Olivin, Wa=Wadsleyite (β-Phase), Sp=Spinell, Pv= Perovskit $(Mg,Fe)SiO_3$, Mw = Magnesiowüstit (Mg,Fe)O. Die gestrichelte Linie ist eine plausible Temperatur-tiefenkurve im Erdmantel.
(b) Variation von seismischem Parameter $\Phi = (v_p^2 - 4/3\, v_s^2)^{1/2}$ und Dichte für verschiedene Metalle aus Stoßwellenexperimenten.

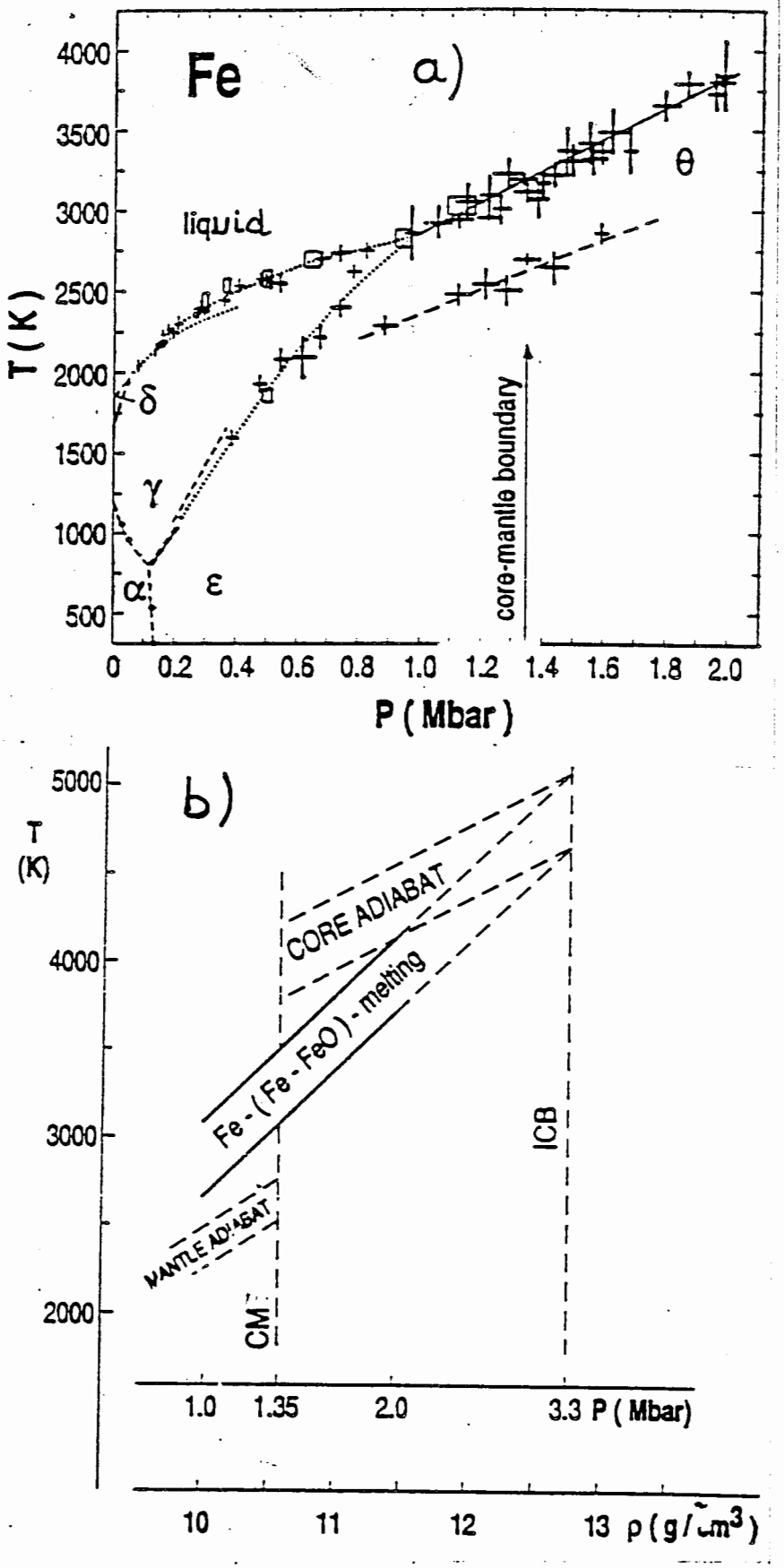

Blatt 20.1 a) Phasendiagramm des Eisens nach Messungen in der Diamantstempelpresse von Boehler.
b) Schematische Darstellung der Berechnung der Kerntemperaturen. Ausgehend vom extrapolierten Schmelzpunkt an der Grenze zum inneren Kern wird ein adiabatischer Temp.-Verlauf im flüssigen äußeren Kern angenommen.

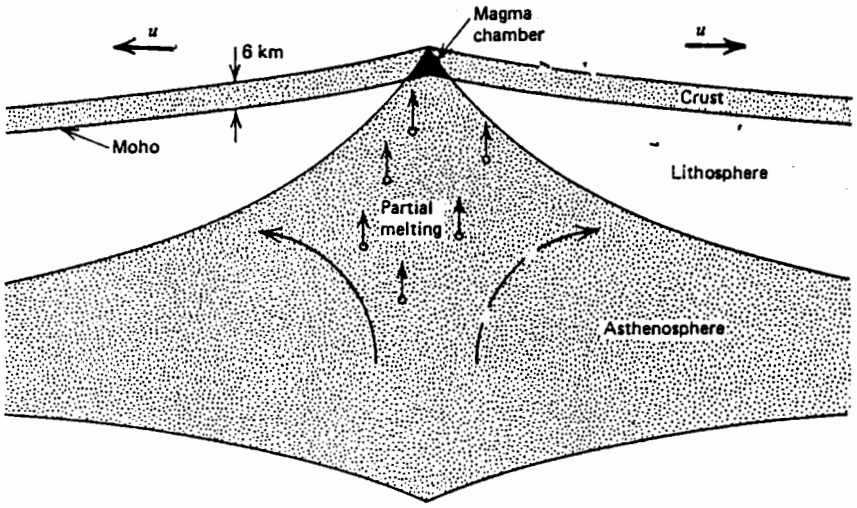

Abb. 3 An accreting plate margin at an ocean ridge.

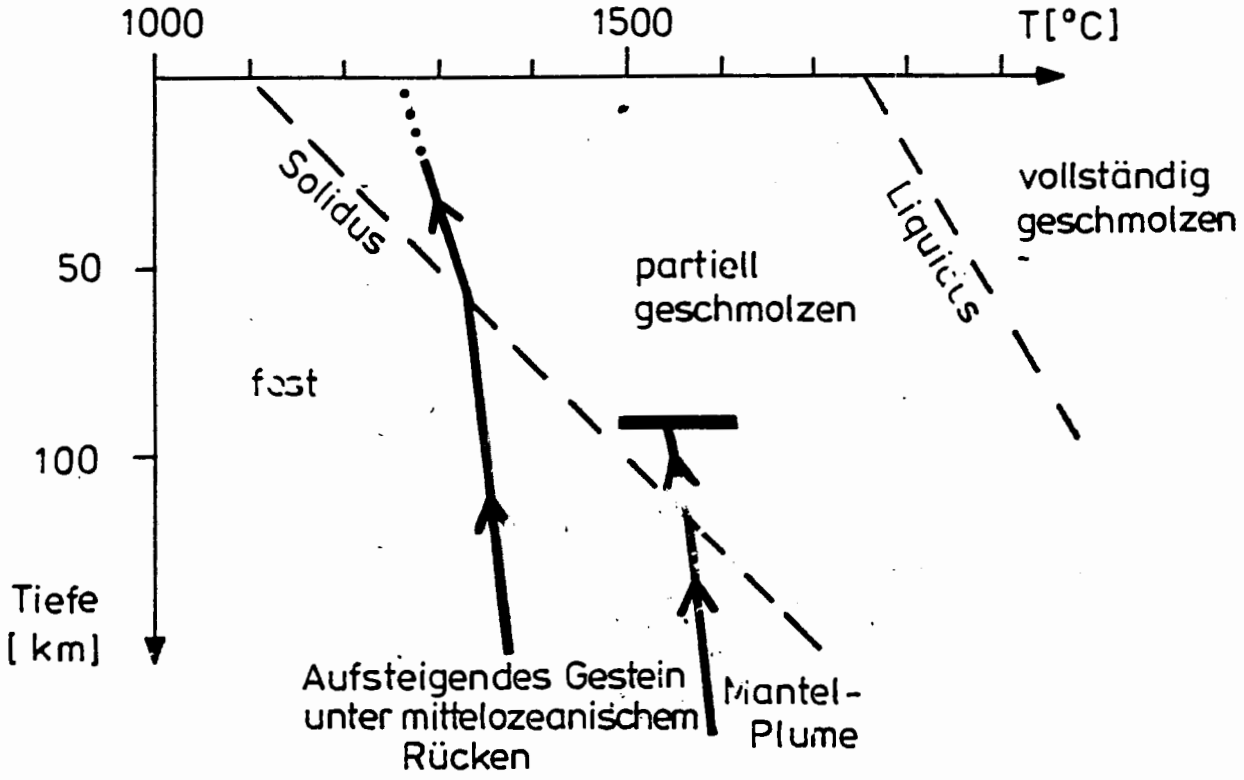

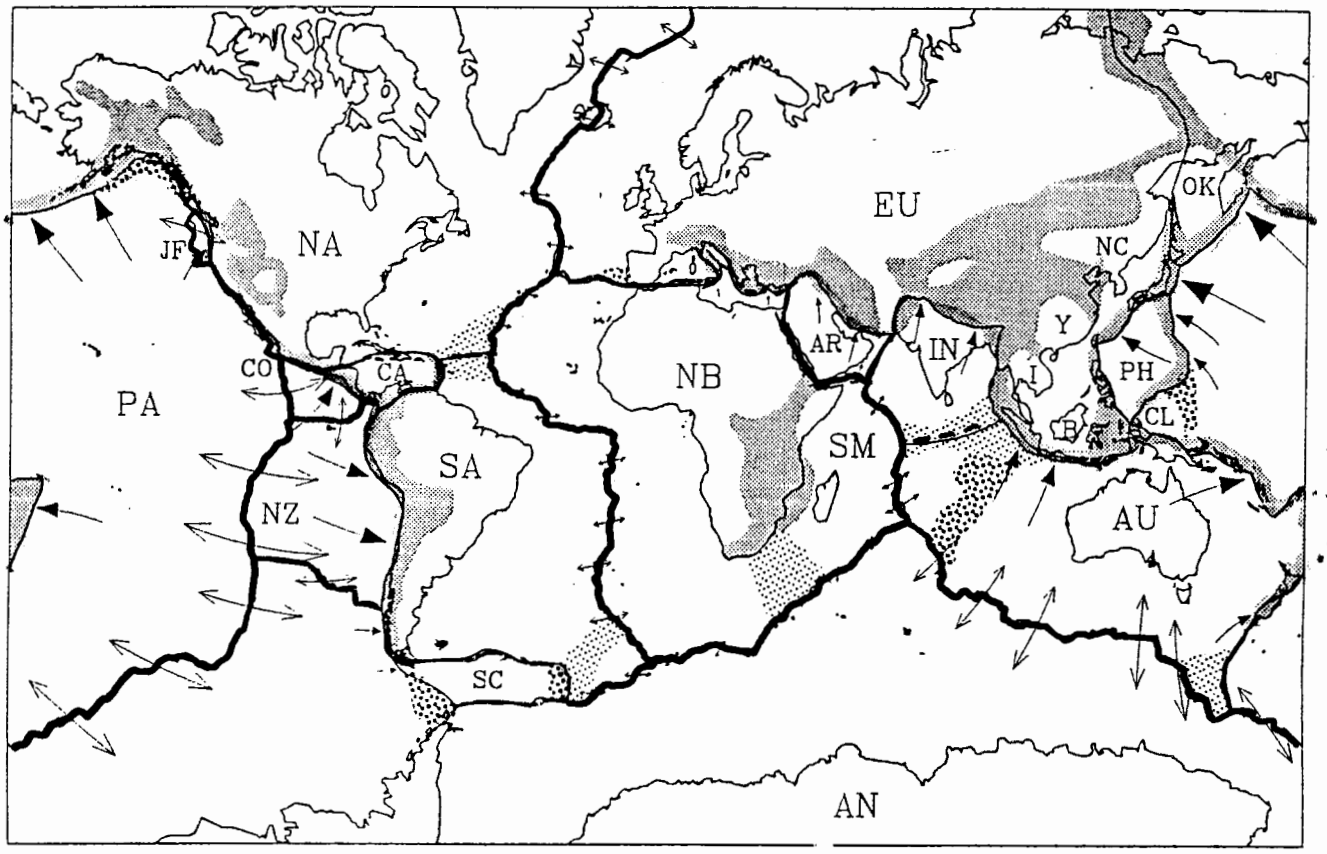

Figure 1. Map showing idealized narrow plate boundaries, velocities between plates, and regions of deforming lithosphere, which can be regarded as diffuse or wide plate boundaries. Plate velocities are shown by arrows. The length of the arrows shows what the displacement would be if the plates were to maintain their present relative angular velocity for 25 million years. The plate separation rate across mid-ocean ridges is shown by symmetrical diverging arrows with unclosed arrowheads at both ends. The plate convergence rate is shown by asymmetrical arrows with one solid arrowhead, which are shown on the underthrust plate where convergence is asymmetric and the polarity is known. Each convergence arrow points toward the overthrust plate. The outlines of deforming regions are approximate and the existence of some deforming zones is speculative. Separate small plates or blocks are labeled in southeast Asia, but their uncertainly located and possibly nonexistent boundaries are not shown in their entirety. Fine stipple shows mainly subaerial regions where the deformation has been inferred from seismicity, topography, other evidence of faulting, or some combination of these. Medium stipple shows mainly submarine regions where the nonclosure of plate circuits indicates measurable deformation; in most cases these zones are also marked by earthquakes. Coarse stipple shows mainly submarine regions where the deformation is inferred mainly from the occurrence of earthquakes. These deforming regions, which constitute wide plate boundaries, cover ~15% of Earth's surface. Future observations may demonstrate that deforming lithosphere covers an area larger or smaller than shown here. Idealized plate boundaries (solid curves) are after *Argus and Gordon* [1991] with the addition of the Scotia plate and several other minor changes. Plate abbreviations: B, Borneo; AN, Antarctica; AR, Arabia; AU, Australia; CA, Caribbean; CL, Caroline; CO, Cocos; EU, Eurasia; I, Indo-China; IN, India; JF, Juan de Fuca; NA, North America; NB, Nubia; NC, North China; NZ, Nazca; OK, Okhotsk; PA, Pacific; SA, South America; SC, Scotia Sea; SM, Somalia; Y, Yangtze. Modified with permission from *Gordon and Stein* [1992, p. 334].

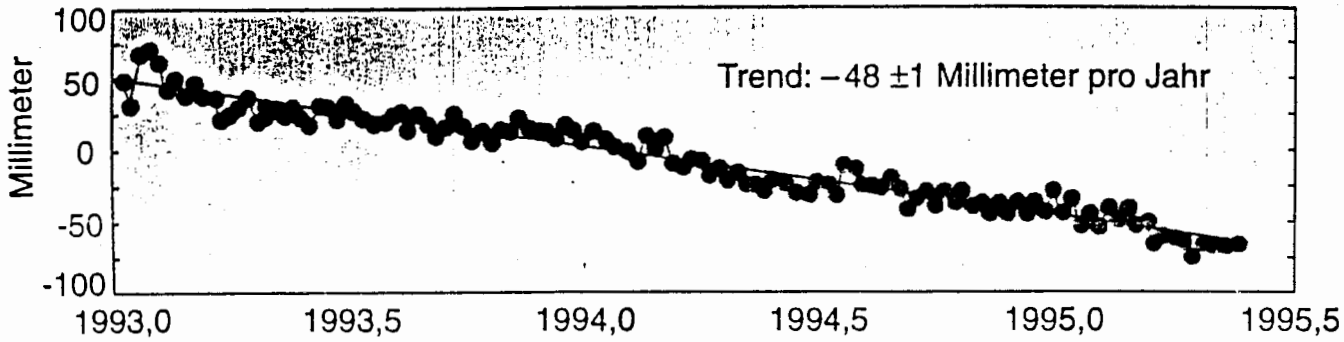

Bild 2: Streckenänderung zwischen Kokee Bay auf Hawai und Fairbanks in Alaska, abgeleitet aus wöchentlichen Messungen der Stationskoordinaten. Die Daten streuen im Mittel acht Millimeter um die berechnete Gerade. Demnach bewegen sich die Stationen aufgrund der Plattentektonik pro Jahr 48 Millimeter aufeinander zu.

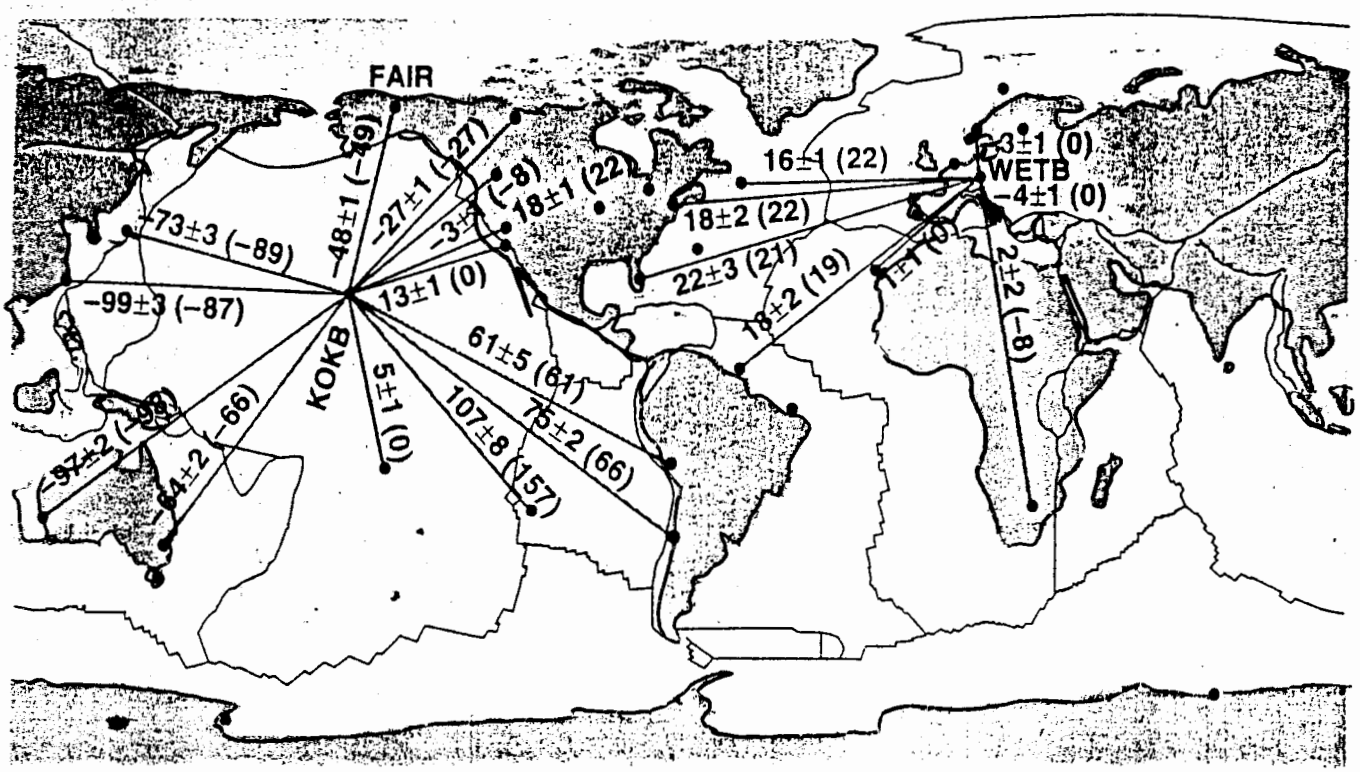

Bild 3: Änderungen der Streckenlänge zwischen Kokee Bay auf Hawai (KOKB) beziehungsweise Wettzell im Bayerischen Wald (WETB) und benachbarten Stationen von Januar 1993 bis Mai 1995 in Millimetern pro Jahr (mit dem geophysikalischen Modell NUVEL berechnete Werte in Klammern, Plattenumrisse in schwarz).

Spektrum 1/96 S. 116

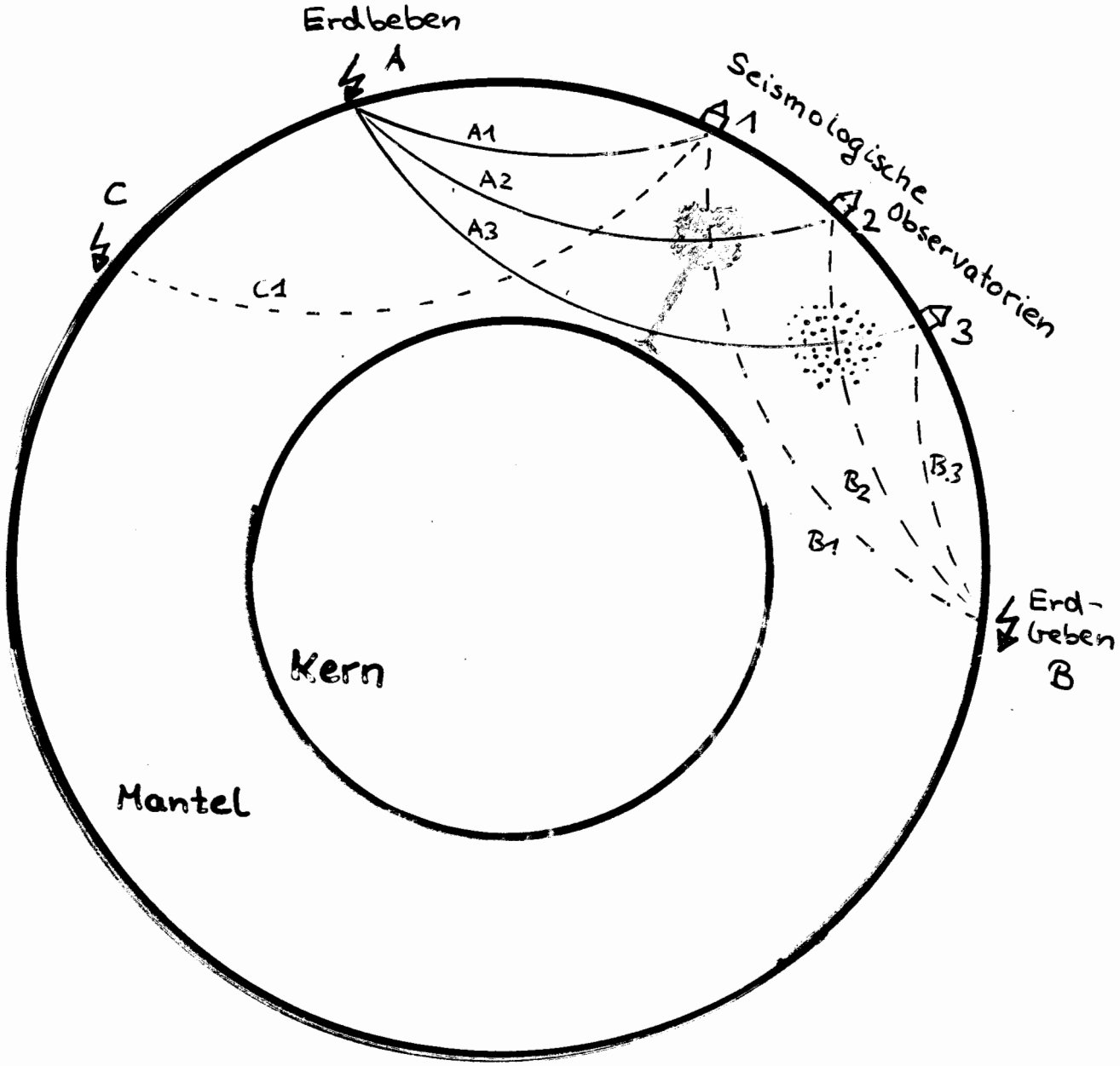

Seismische Tomographie

Earth's structure at 1300 km depth

Tomography: Widiyantoro & Van der Hilst (1996)

Data: Engdahl, Van der Hilst, & Buland (1996)

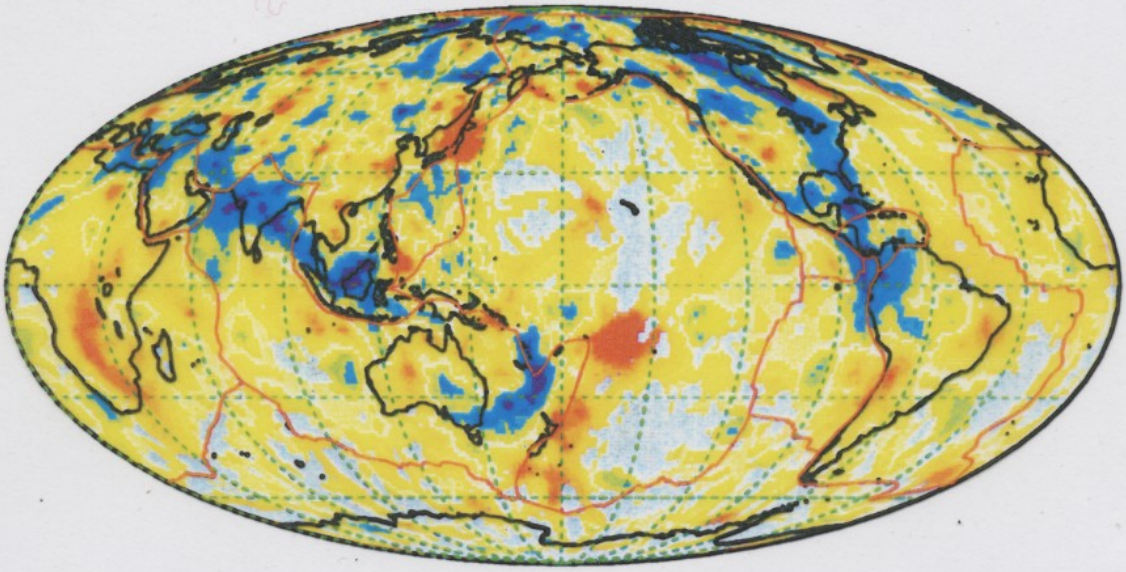

Plate convergence during past 109 Ma

Sources: Gordon & Jurdy (1986) and Lithgow-Bertelloni & Richards (1996)

(Compilation by Steinberger (1996))

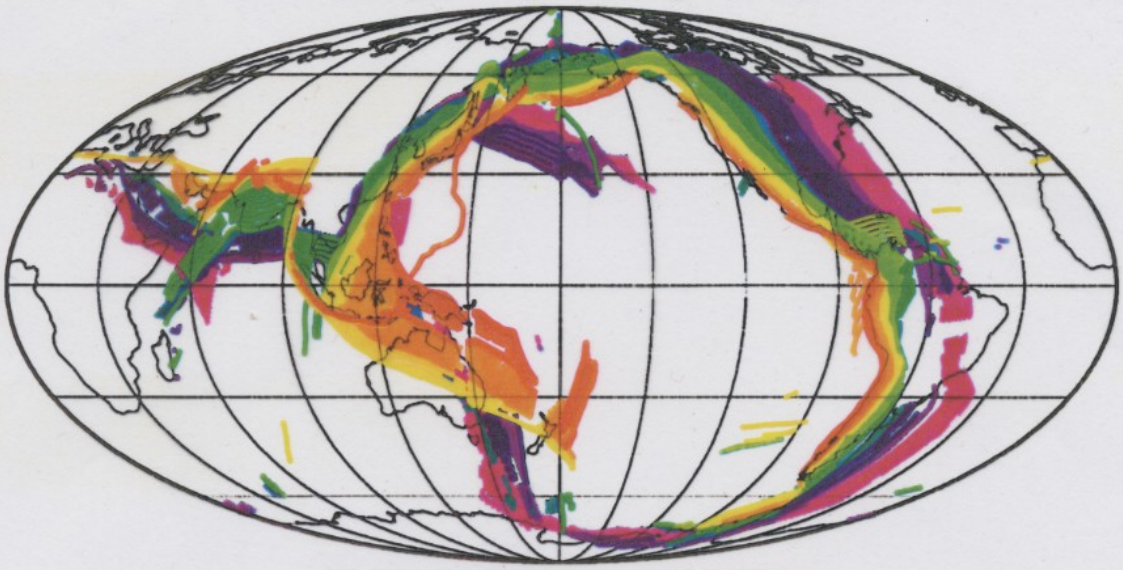

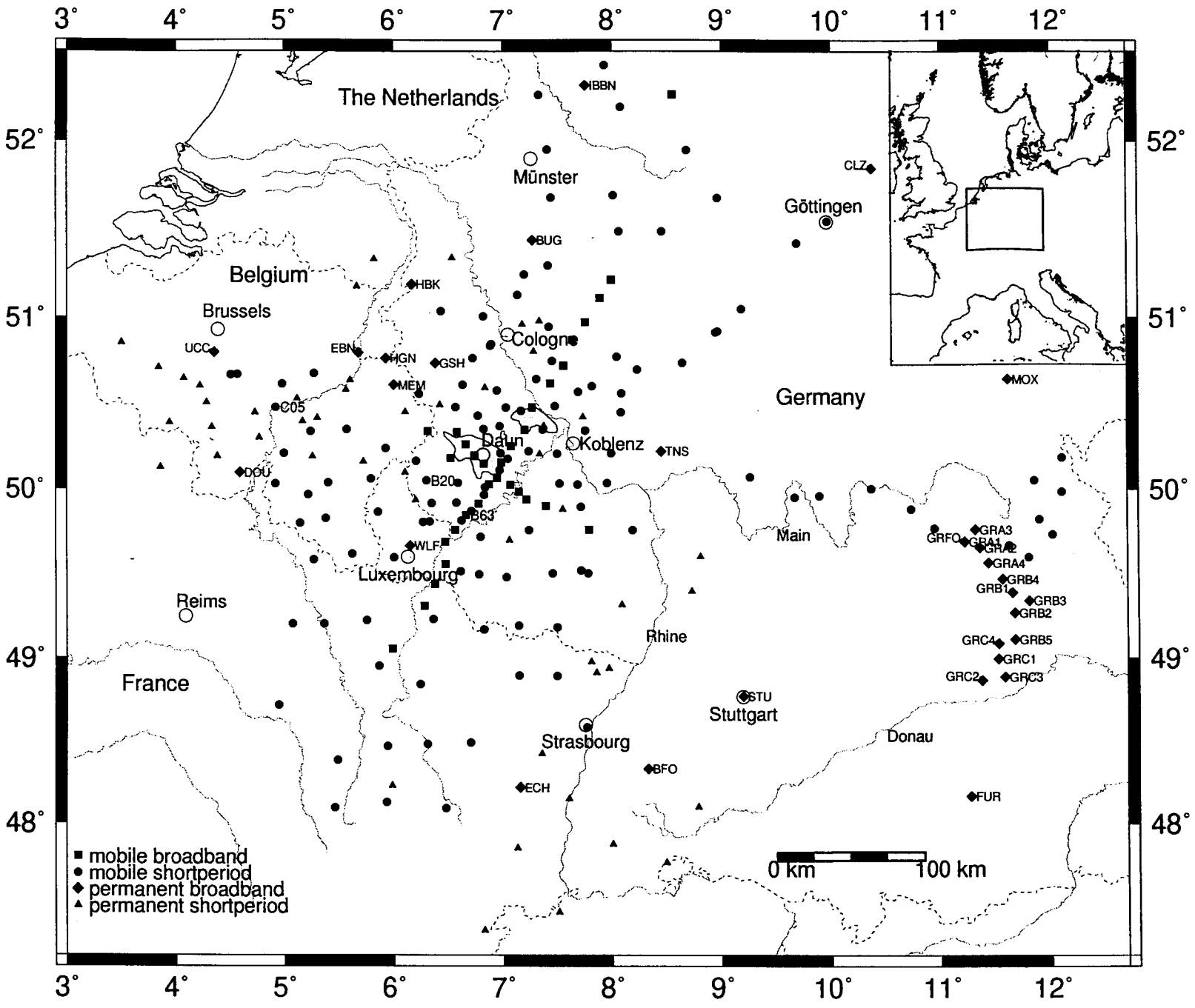
3°
4°
5°
6°
7°
8°
9°
10°
11°
12°
52°
51°
50°
49°
48°
The Netherlands
Belgium
Brussels
France
Reims
Luxembourg
Münster
Cologne
Göttingen
Germany
Daun
Koblenz
Main
Rhine
Stuttgart
Strasbourg
Donau
IBBN
BUG
HBK
UCC
EBN
HGN
GSH
MEM
C05
DOU
B20
B63
WLF
TNS
CLZ
MOX
GRFO
GRA3
GRA1
GRA2
GRA4
GRB4
GRB1
GRB3
GRB2
GRC4
GRB5
GRC1
GRC2
GRC3
STU
BFO
ECH
FUR
mobile broadband
mobile shortperiod
permanent broadband
permanent shortperiod
0 km
100 km

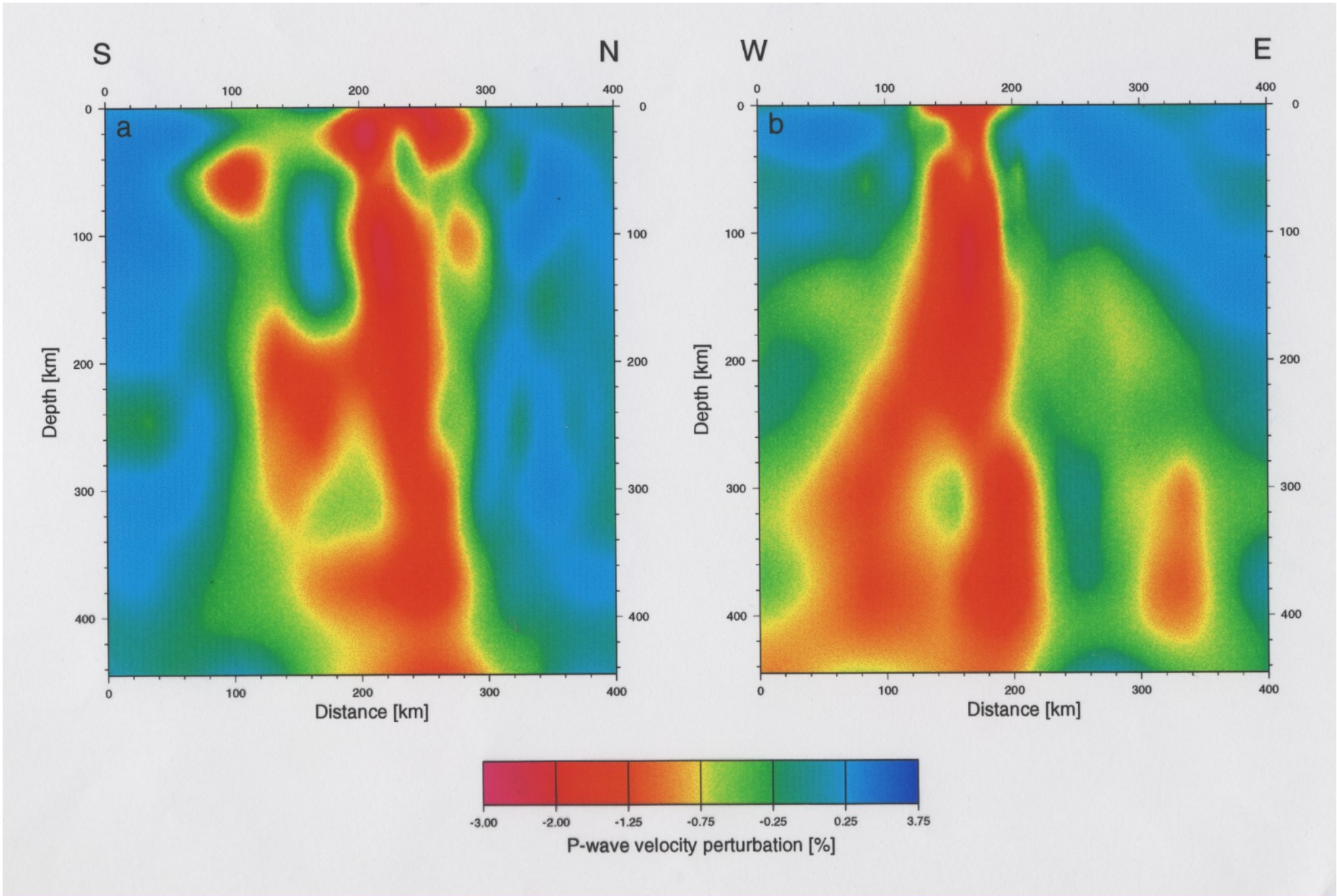
S
N
a
Depth [km]
Distance [km]
0
100
200
300
400
W
E
b
Depth [km]
Distance [km]
-3.00
-2.00
-1.25
-0.75
-0.25
0.25
3.75
P-wave velocity perturbation [%]